communications physics

ARTICLE

https://doi.org/10.1038/s42005-022-01115-7 OPEN

Evidence of entropy cascade in collisionless magnetized plasma turbulence

Eiichirou Kawamori[1]✉ & Yu-Ting Lin[1,2]

The turbulence of collisionless magnetized plasmas, as observed in space, astrophysical, and magnetically confined fusion plasmas, has attracted considerable interest for a long-time. The entropy cascade in collisionless magnetized plasmas is a theoretically proposed dynamics comparable to the Kolmogorov energy cascade in fluid turbulence. Here, we present evidence of an entropy cascade in laboratory plasmas by direct visualization of the entropy distribution in the phase space of turbulence in laboratory experiments. This measurement confirms the scaling laws predicted by the gyrokinetic theory with the dual self-similarity hypothesis, which reflects the interplay between the position and velocity of ions by perpendicular nonlinear phase mixing. This verification contributes to our understanding of turbulent heating in the solar corona, accretion disks, and magnetically confined fusion plasmas.

---

[1] Institute of Space and Plasma Sciences, National Cheng Kung University, Tainan, Taiwan. [2] Present address: Graduate School of Frontier Sciences, The University of Tokyo, Tokyo, Japan. ✉email: kawamori@isaps.ncku.edu.tw

The spectral universality in seemingly case-dependent fluid turbulence, which reflects self-similar dynamics in the inertial range of an energy cascade, is one of the most surprising findings in modern physics[1–3]. The presence or absence of universality in collisionless magnetized plasma turbulence exemplified by space, astrophysical, and magnetically confined fusion plasmas has been explored out of scientific interest. This question not only comes out of pure scientific curiosity but is also strongly associated with important practical problems, so-called turbulent heating in the solar wind[4,5], solar corona[6,7], accretion disks[8–10], and energy transport in magnetically confined fusion plasmas[11–13]. These problems raise the question: at which scales are ions accelerated and thermalized? Some examples of turbulent heating include the coronal heating problem and the nonadiabatic temperature evolution of the solar wind[6]. One of the major models for explaining the heating mechanisms of the high-temperature corona/solar wind is the wave turbulence heating model (one is the microflare/nanoflare theory). The energy flux of the Alfvén waves/kinetic Alfvén waves propagating from the solar photosphere and chromosphere into the corona is considered to be sufficient to heat the corona temperature up to the observed temperature of ~100 eV. However, this model encounters a complicated problem of what mechanisms (exemplified by ion cyclotron resonance, Alfvén resonance, linear phase mixing, and shock dissipation, among many others) are responsible for dissipating (partitioning) the wave energy of the Alfvén wave/kinetic Alfvén wave turbulence. The entropy cascade attributed to nonlinear phase mixing is a compelling hypothesis[4] for the mechanism. This hypothesis motivates us to experimentally study the validity of the entropy cascade via nonlinear phase mixing.

According to Boltzmann's H-theorem, entropy production, in other words, ion heating, is realized only by collisions in weakly collisional (collisionless) plasmas at the microscopic scale[14] much smaller than the ion gyro-scales (the inner scale) with a significant $\partial f/\partial \boldsymbol{v}$ or $\partial^2 f/\partial \boldsymbol{v}^2$, where f and $\boldsymbol{v}$ are the ion velocity distribution function and the velocity vector of ions, respectively. However, macroscopic scales are typical energy inputs to the system (the outer scale), which are considerably separated from the dissipation scales (the inner scale). This fact strongly indicates that the injected energy is nonlinearly transferred as free energy (≈ negative signed entropy) from the outer scale to the inner scale in collisionless magnetized plasmas. This process is called an entropy cascade[14–16]. The gyrokinetic theory[15,17,18] predicts that the nonlinear phase-mixing[19] is responsible for the transfer of entropy in the inertial subrange[14,20], and has been confirmed in a number of gyrokinetic numerical simulations regardless of two-dimensional (2D) electrostatic[16] or three-dimensional (3D) electrostatic[21] or electromagnetic turbulence[4,22,23]. In addition, in a real plasma, an indication of a free energy cascade was observed in electromagnetic turbulence in the Earth's magnetosheath as fine-scale structures in the ion velocity distribution functions[24]. Regardless of the fact that the original concept of the entropy cascade by the nonlinear phase mixing considers only 2D electrostatic fluctuations[14,19], signatures of the entropy cascade have been witnessed in magnetized plasma turbulence in various situations. This broad applicability of the entropy cascade picture to a wide range of collisionless magnetized plasma turbulence is attributed to the fact that turbulence of collisionless magnetized plasmas universally consists of highly anisotropic fluctuations with frequencies much lower than the ion cyclotron frequency in addition to the intrinsic electrostatic nature of perpendicular fluctuations.

Nonlinear phase mixing is a phase-randomizing mechanism of electrostatic fluctuations of quasi-2D magnetized plasmas by a finite-Larmor radius effect[19]. It couples ion dynamics in the position and the velocity spaces, resulting in entropy cascades in the phase space[14,25].

Although the visualization of the entropy distribution in the phase space of ions has been implemented in some simulations[25,26], no measurements have been conducted in real plasmas, including space and laboratory plasma experiments.

The gyrokinetic theory for treating gyroscale plasma phenomena considers kinetics of 'charged rings' of gyrating ions, whose statistics are represented by ring-averaged ion velocity distribution functions at a fixed guiding center. The gyrokinetic system is invariant under the scaling transformation; $(g, \phi, \mathbf{r}, v_\perp) \rightarrow (g, \mu^2\phi, \mu\mathbf{r}, \mu v_\perp)$, where g, ϕ, $\mathbf{r}$, $v_\perp$, and μ are fluctuation components of the ring-averaged ion velocity distribution function, the electrostatic potential, the space coordinate, the perpendicular velocity of ions, and a scaling factor, respectively[20]. Note that $g(\mathbf{R}, v_\perp)$ is the gyro average of $\delta f = f(\mathbf{r}, \mathbf{v}, t) - F_0(\mathbf{r}, \mathbf{v})$, which is the perturbed distribution function, where F_0 is the background equilibrium distribution function that is steady on the timescale of turbulent fluctuations (a Maxwellian is assumed in the standard gyrokinetic theory), and $\mathbf{R}$ is the fixed guiding center position.

The dual self-similarity hypothesis for the position and velocity spaces based on the above scale invariance predicts the power laws of spectra of the free energy $W_{g1} = \iint \frac{g(\mathbf{R}, v_\perp)^2}{2} dv_\perp d\mathbf{R}$ and energy $E_g = \frac{1}{2}\int \tilde{\phi}(\mathbf{r})^2 d\mathbf{r}$ with the use of $g(\mathbf{R}, v_\perp)$ for the 2D electrostatic turbulence. The dual self-similar dynamics in the phase-space are expected to be accompanied by a dual cascade of two kinds of turbulence energy in 2D electrostatic turbulence: the forward cascade of free energy and an inverse cascade of electrostatic energy[25]. This dual self-similarity hypothesis extends the renowned Kolmogorov self-similarity hypothesis in fluid turbulence[27] to the phase space of ions in gyrokinetic turbulence. It argues that the turbulent behavior of ions at the sub-Larmor scales is independent of scale in both their position and velocity spaces. These are strongly coupled in the phase space by nonlinear phase mixing.

Therefore, in this experiment, we employed diagnostic instruments named Ring-averaged ion velocity distribution function probes (RIDFPs)[28] to measure $g(\mathbf{R}, v_\perp)$ for evaluation of the theoretically predicted power laws. Although our previous paper[29] showed agreement between measurements and the theoretical prediction on the power spectrum of E_g as a function of the fluctuation wavenumber perpendicular to the background magnetic field $k_\perp$, we still face a lack of information on the velocity space to conclude the validity of the dual-cascade theory of gyrokinetic turbulence.

Here, we show the direct visualization of the entropy distribution of ions in the phase space of laboratory-magnetized plasma turbulence. These results provide the evidence of the existence of dual self-similarity and the dual cascade of entropy and field energy in the phase space of turbulence.

Results and discussion

Experimental setup. In this experiment ("Methods": Magnetized plasma experiment (MPX) device, ring-averaged ion velocity distribution function probes, other measurement tools, and the plasma parameters), we prepared four states of electrostatic 2D turbulence driven by resistive drift-waves having varied driving perpendicular wavenumbers $k_{\mathrm{drive}}\rho_{\mathrm{thi}}$ between ~0 and 10 with control of the density of the background neutral particles, where ρ_{thi} is the Larmor radius of ions at the thermal velocity v_{thi}. While this control scheme of $k_{\mathrm{drive}}\rho_{\mathrm{thi}}$ is not a well-established technique, we prepared the turbulent states with the control of the neutral particle density with reference to the numerical work[30], which describes the numerical investigation results of an energy partition of turbulence in a cylindrical plasma. We use Fourier–Hankel components of the free energy: $W_{g1}(k_\perp, p) \equiv p\sum_{|\mathbf{k}_\perp|=k_\perp}|g(\mathbf{k}_\perp, p)|^2 = \pi k_\perp p|g(k_\perp, p)|^2$, where $g(k_\perp, p)$ is the Fourier–Hankel transform of $g(\mathbf{R}, v_\perp)$ concerning the guiding center position and the ion velocity[20], and the parameter p indicates the reciprocal of the fluctuation scale of $g(\mathbf{R}, v_\perp)$ in the velocity direction corresponding to the wavenumber in the velocity space.

The gyrokinetic approximation requires $\omega \ll \Omega_{\rm ci}$, where ω and $\Omega_{\rm ci}$ are the wave frequencies and the ion cyclotron frequency, respectively. The higher the axial magnetic field strength is, the more improved the gyrokinetic condition. However, our experiment does not completely satisfy $\omega \ll \Omega_{\rm ci}$ ($\omega/2\pi \sim 0.1$–4 kHz, $\Omega_{\rm ci}/2\pi = 8.4$ kHz), which is a consequence of the two following adverse impacts of the strong field on our plasma states: (i) the suppression of the excitation of the drift waves; in our plasmas, the high magnetic field stabilizes the drift waves because of a change in the radial profile of the density; and (ii) the reduction of the ion gyro-radius, which limits the performance of the diagnostic. In other words, the axial magnetic field strength is set at a weak value to fully use all the velocity channels of the RIDFPs by expanding the ion gyro radii. This improves the resolution of the RIDFP measurement in the velocity space. In the third paragraph from the end of this section, we explain the influence of this incomplete satisfaction of the gyrokinetic ordering on the interpretation of the experimental results.

Spectra of free energy in the *k*–*v* space. Figure 1 shows time-averaged free energy spectra $k_\perp|g(k_\perp, v_\perp)|^2$ as functions of $k_x\rho_{\rm thi}$ and $v_\perp$ up to ~$2v_{\rm thi}$ for (Fig. 1a) $k_{\rm drive}\rho_{\rm thi} \sim 1$ (W_{g1} injection at large scales) and (Fig. 1b) $k_{\rm drive}\rho_{\rm thi} \sim 10$ (W_{g1} injection at small scales), respectively. We regard $k_x \approx k_\perp$ in evaluating $k_\perp|g(k_\perp, v_\perp)|^2$ based on the assumption of isotropy and fast decay of $|g(k_\perp, v_\perp)|^2$ for $k_\perp$. The factor $k_\perp$ indicates the circumferential length in the $\mathbf{k}_\perp$-space.

$k_\perp|g(k_\perp, \boldsymbol{v}_\perp)|^2$ for (A) $k_{\rm drive}\rho_{\rm thi} \sim 1$ exhibits, in the entire range of $v_\perp$, the large amplitude at $k_x\rho_{\rm thi} \sim 1-2$ consistent with $|\tilde{\phi}_{\rm f}(f, k_y)|^2$ measured by a fine-scale Langmuir probe (FSLP) for $k_{\rm drive}\rho_{\rm thi} \sim 1$ (Fig. 2a), which shows excitation of $k_x\rho_{\rm thi} \sim 1$ components at $f \sim 1.0-1.3$ kHz. Accordingly, the low $k_\perp$ components at $k_x\rho_{\rm thi} \sim 1$–2 show variation in the $v_\perp$-direction at the scale of ~$v_{\rm thi}$ in Fig. 1a. The amplitude of components for $|k_x\rho_{\rm thi}| > 2$ decays in large k_x with finer-scale variation in the $v_\perp$-direction. On the other hand, $k_\perp|g(k_\perp, v_\perp)|^2$ for (B) $k_{\rm drive}\rho_{\rm thi} \sim 10$ exhibits significant power at $|k_x\rho_{\rm thi}| > 10$. These $|k_x\rho_{\rm thi}| > 10$ components exhibit structures in the $v_\perp$-direction at sub-$v_{\rm thi}$ scales. This indicates strong coupling between the position and velocity spaces. See the next subsection for a quantitative assessment of scales in $v_\perp$ space using spectra.

Comparison with theory. In the second–fourth rows of Fig. 2, we show variation in the spectra of the collisionless invariants of 2D electrostatic gyrokinetics, $W_{g1}(k_\perp, p)$ and $E_g(k_\perp)$, for varied $k_{\rm drive}\rho_{\rm thi}$ approximately between 0 and 10, (the first column) $k_{\rm drive}\rho_{\rm thi} \sim 1$, (the second column) $k_{\rm drive}\rho_{\rm thi} \sim 3-4$, (the third column) $k_{\rm drive}\rho_{\rm thi} \sim 0$–$4$, and (the fourth column) $k_{\rm drive}\rho_{\rm thi} \sim 10$. These values of $k_{\rm drive}\rho_{\rm thi}$ are evaluated from $|\tilde{\phi}_{\rm f}(f, k_y)|^2$ measured by FSLP as shown in the first row of Fig. 2a–d. In the respective cases of different $k_{\rm drive}\rho_{\rm thi}$, the following two distinct frequency bands can be identified in $|\tilde{\phi}_{\rm f}(f, k_y)|^2$: one showing significant power with nonstatistical/deterministic distribution corresponding to the drive, for example, $k_y\rho_{\rm thi} \sim 1$ component at $f \sim 1.3$ kHz in Fig. 2a ($k_y\rho_{\rm thi} \sim 3$–4 component at $f \sim 1.7$ kHz in Fig. 2b, and $k_y\rho_{\rm thi} \sim 10$ component at $f \sim 3$–4 kHz in Fig. 2d), and the other bands showing scattered, statistical distribution in the k_y-direction corresponding to turbulent cascade. Nonlinear dynamics exhibited in these shots are local because no nonlocal resonant wave–wave interactions occurred except for the $k_{\rm drive}\rho_{\rm thi} \sim 0$–$4$ state (the vertical array of Fig. 2c, g, k and o), which exhibits a continuous driving spectrum in the f-$k_y\rho_{\rm thi}$ diagram and is a turbulent state originating from a nonlinear coherent state of drift waves called solitary drift waves[31].

The plots shown in the second row (Fig. 2e–h) are $W_{g1}(k_\perp, p)$ (negative signed entropy) in the $k_\perp$-p space, namely, position–velocity space (see "Evaluation of 1D spectrum of free energy $W_{g1}{}^{\rm 1D}(k_x, p)$ and relationship with $W_{g1}(k_\perp)$ and $W_{g1}(p)$" in Methods). In the following results of varied $k_{\rm drive}\rho_{\rm thi}$, a position of the drive moves along the diagonal in the $k_\perp$-p space, as shown in Fig. 2e–h.

When W_{g1} is injected at large scales (Fig. 2e), in which a significant power of W_{g1} can be seen at the left bottom of the diagram at $k_\perp\rho_{\rm thi} \sim pv_{\rm thi} \sim 1$–$4$ corresponding to $k_{\rm drive}\rho_{\rm thi}$, W_{g1} broadly develops along the diagonal from the driving scale toward the upper-right direction, reaching the top right corner around $k_\perp\rho_{\rm thi} \sim pv_{\rm thi} \sim 20$. (A similar profile can be seen in Fig. 6 in the article by Tatsuno et al.[26]). According to the gyrokinetic Poisson Eq., the potential fluctuation $\tilde{\phi}(\mathbf{k}_\perp)$ is generated solely by nonlinear phase mixing, that is, $g(k_\perp, p = k_\perp)$ (Eq. (2.11) in the article by Plunk et al.[20]). This provides a Fjørtoft-type relationship $W_{g1}(k_\perp, p = k_\perp) = k_\perp E_g(k_\perp)$ (Eq. (7.14) in the article by Plunk et al.[20]). Therefore, diagonal transport of W_{g1} in the $k_\perp$-p space is inevitable when a dual-cascade of W_{g1} and E_g occurs.

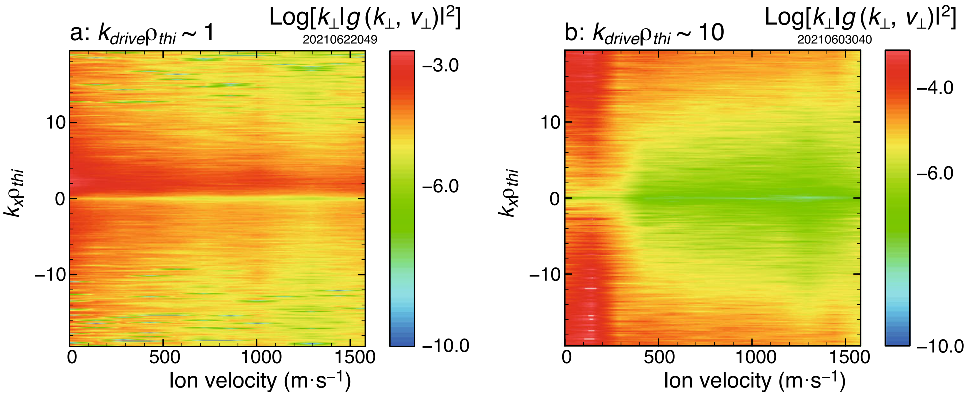

Fig. 1 Spectra of free energy in the wavenumber-velocity space. Time-averaged power spectra $k_\perp|g(k_\perp, v_\perp)|^2$ measured by RIDFPs as functions of the wavenumber k_x normalized by the ion Larmor radius $\rho_{\rm thi}$ at the thermal velocity $v_{\rm thi}$ and the perpendicular ion velocity $v_\perp$ up to ~$2v_{\rm thi}$ for **a** driving perpendicular wavenumbers $k_{\rm drive}\rho_{\rm thi} \sim 1$ and **b** $k_{\rm drive}\rho_{\rm thi} \sim 10$, respectively.

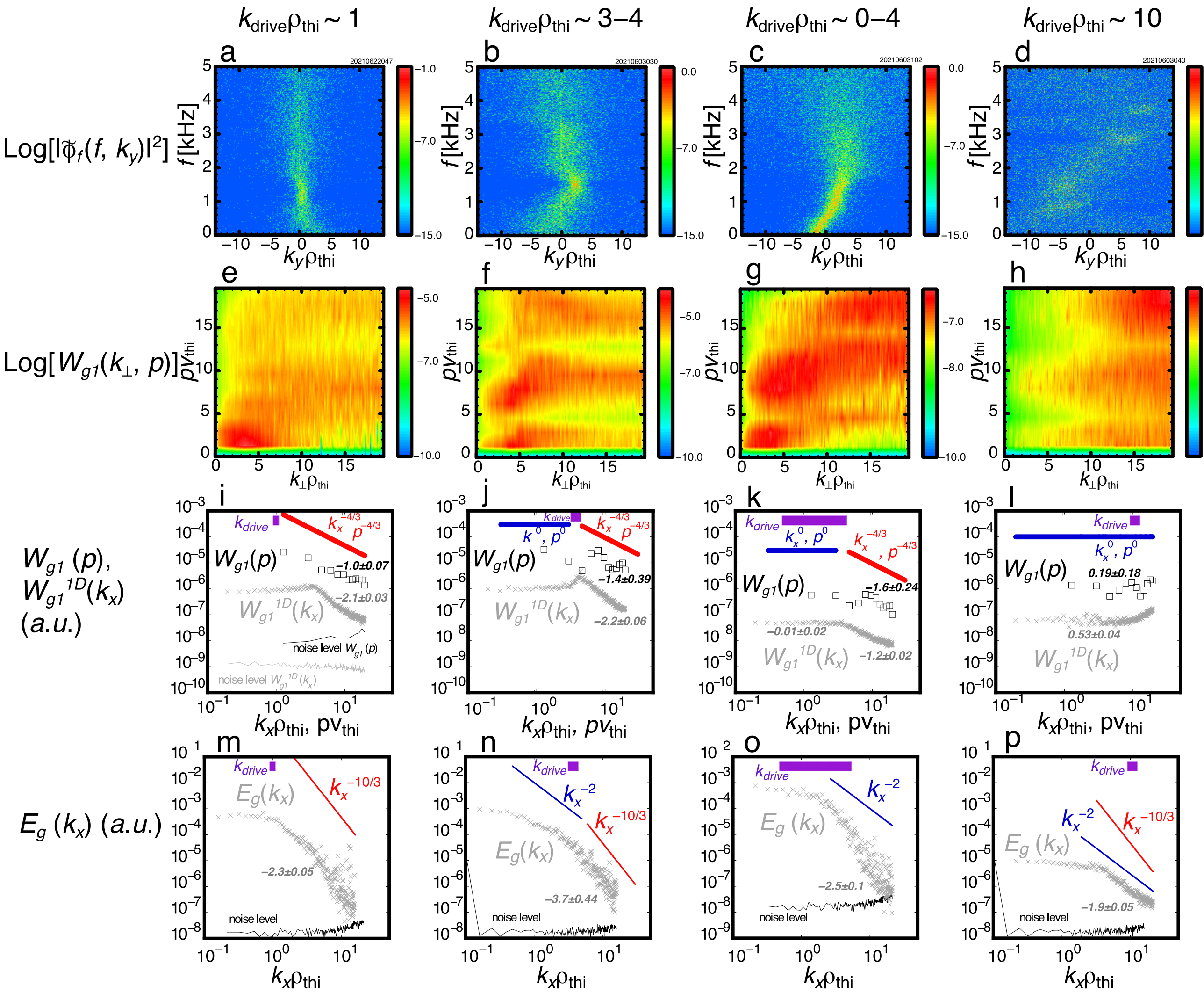

Fig. 2 Variation in spectra of the invariants of gyro-kinetics. The free energy $W_{g1}(k_{\perp}, p)$ and the electrostatic energy $E_g(k_{\perp})$ for varied driving perpendicular wavenumbers $k_{\rm drive}\rho_{\rm thi}$ between ~0 and 10, (the 1st column) $k_{\rm drive}\rho_{\rm thi}$ ~ 1, (the 2nd column) $k_{\rm drive}\rho_{\rm thi}$ ~ 3−4, (the 3rd column) $k_{\rm drive}\rho_{\rm thi}$ ~ 0−4, and (the 4th column) $k_{\rm drive}\rho_{\rm thi}$ ~ 10, respectively. The plots in the 1st row (**a**–**d**) are the power spectra of potential fluctuation $|\tilde{\phi}_f(f, k_x)|^2$ measured by FSLP. The plots shown in the 2nd row (**e**–**h**) are $W_{g1}(k_{\perp}, p)$ in the $k_{\perp}$- p-space, namely, position–velocity-space. The 3rd row (**i**–**l**) are (cross) 1D spectra $W_{g1}{}^{1D}$ of the free energy as functions of $k_x\rho_{\rm thi}$ and (open square) p-spectra of $W_{g1}(p)$, respectively. $E_g(k_{\perp})$ spectra are shown in the 4th row (**m**–**p**). Respective $k_{\rm drive}\rho_{\rm thi}$ ranges are shown by purple color bars. The blue and red bars represent power laws predicted by the gyrokinetic theory[20] for (blue) $k_{\perp} < k_{\rm drive}$ and (red) $k_{\perp} > k_{\rm drive}$, respectively.

This $W_{g1}(k_{\perp}, p)$ spectrum exhibits the generation of W_{g1} at finer scales than the drive. This indicates that the nonlinear phase mixing works, resulting in a forward cascade of W_{g1}. This cascading nature will be examined below by comparing their power laws obtained from the measurement and the theory.

As $k_{\rm drive}\rho_{\rm thi}$ increased to ≈10, as shown in Fig. 2f–h, the significant W_{g1} part moved in the upper-right direction along the diagonal line toward higher $k_{\perp}\rho_{\rm thi} \sim pv_{\rm thi}$ locations corresponding to the increase in $k_{\rm drive}\rho_{\rm thi}$. In all the cases of $k_{\rm drive}\rho_{\rm thi}$ (Fig. 2e–h), the spread of $W_{g1}(k_{\perp}, p)$ along with the diagonal directions (between the bottom left and the upper right) is obvious. In these cases, the Fjørtoft-type energetic transition[25], namely, a transition involving only diagonal components, can be realized.

In the third row of Fig. 2i–l), (crosses) one-dimensional (1D) spectra $W_{g1}{}^{\rm 1D}$ of the free energy as functions of $k_x\rho_{\rm thi}$ and (open squares) p-spectra of $W_{g1}(p)$, respectively, are shown. Note that when $W_{g1}(k_{\perp}) \propto k_{\perp}{}^{-\alpha}$, $W_{g1}{}^{\rm 1D}(k_x) \propto k_x{}^{-\alpha}$ (see "Evaluation of 1D spectrum of free energy $W_{g1}{}^{\rm 1D}(k_x, p)$ and relationship with $W_{g1}(k_{\perp})$ and $W_{g1}(p)$" in Methods). Respective $k_{\rm drive}\rho_{\rm thi}$ ranges are shown by purple bars. The blue and red bars represent the power laws predicted by the gyrokinetic theory for (blue) the inverse-cascade range $k_{\perp} < k_{\rm drive}$ and (red) the forward cascade range $k_{\perp} > k_{\rm drive}$, respectively[20]. The respective power indices of $W_{g1}{}^{\rm 1D}(k_x)$ and $W_{g1}(p)$ evaluated from the least-square fitting to the measured data points are indicated by numbers with the standard errors (*SE*). The noise levels of $W_{g1}{}^{\rm 1D}(k_x)$ and $W_{g1}(p)$ estimated from a vacuum shot are included in Fig. 2i. $W_{g1}(p)$ in Fig. 2i (injection at a large scale) shows power-law decay starting at $k_x\rho_{\rm thi} \sim k_{\rm drive}\rho_{\rm thi} \sim 1$ up to the detection limit of $k_x\rho_{\rm thi} \sim pv_{\rm thi} \sim 20$, clearly indicating the existence of an inertial subrange of the entropy (free energy). The evaluated exponent for the measured $W_{g1}(p)$, -1.0, approximately agrees with the theoretical value of $-4/3$ within 5 times *SE*. For smaller scales $k_x\rho_{\rm thi} > 3$, $W_{g1}{}^{\rm 1D}(k_x)$ in Fig. 2i shows a similar decaying tendency to $W_{g1}(p)$, which is a strong indication of the dual self-similarity dynamics, although the discrepancy of $W_{g1}{}^{\rm 1D}(k_x)$ from the theoretical exponent is larger than 25 times *SE*. Larger discrepancies between the theoretical exponents and the measured ones in $W_{g1}{}^{\rm 1D}(k_x)$ than those in $W_{g1}(p)$ are seen in all cases of $k_{\rm drive}$.

As $k_{\rm drive}\rho_{\rm thi}$ increases to 3–4 (Fig. 2j), $W_{g1}(p)$ shows an inflection point at $k_x\rho_{\rm thi} \sim k_{\rm drive}\rho_{\rm thi} \sim 3$–$4$. Correspondingly, $W_{g1}{}^{\rm 1D}(k_x)$ follows this change in the spectrum. For an injection at small scales $k_{\rm drive}\rho_{\rm thi} \sim 10$ (Fig. 2l), both $W_{g1}(p)$ and $W_{g1}{}^{1D}(k_x)$ become independent of p and k_x, indicating good agreement with the theory[20]. It should be noted that the decaying exponents of both $W_{g1}{}^{1D}(k_x)$ and $W_{g1}(p)$ at $k_x\rho_{\rm thi} \gg 1$ exhibit similar values in the respective cases of $k_{\rm drive}\rho_{\rm thi}$ and similar variation for varied $k_{\rm drive}\rho_{\rm thi}$ in Fig. 2i–l. This indicates the formation of inertial subranges in both the position and velocity spaces and strong coupling between them. A similar result is obtained in the gyrokinetic simulation[16,26].

In the case of $k_{\rm drive}\rho_{\rm thi} \sim 0$–$4$ (Fig. 2k), despite the driving source in the target k-range (i.e., noninertial range), strong k–p coupling occurs, indicating the universality of nonlinear phase mixing in magnetized plasma turbulence.

The abovementioned approximate agreement between the measurement and the theoretical prediction of $W_{g1}(p)$ and $W_{g1}(k_\perp)$ within $\sim 1-25$ times SE is supported by the $E_g(k_\perp)$ spectra measured by FSLP shown in the fourth row of Fig. 2 (Fig. 2m–p). Note that when $E_g(k_\perp) \propto k_\perp{}^{-\alpha}$, $E_{g1}{}^{1D}(k_x) \propto k_x{}^{-\alpha}$ ("Methods": Evaluation of the 1D spectrum of the electrostatic field energy $E_g{}^{1D}(k_y)$ and its relationship with $E_g(k_\perp)$). The blue and red bars represent the power laws predicted by kinetic theory for (blue) $k_\perp < k_{\rm drive}$ and (red) $k_\perp > k_{\rm drive}$, respectively. The respective power indices of $E_{g1}{}^{1D}(k_x)$ evaluated from the least-square fitting to the measured data points are indicated aside by numbers with the standard errors. The noise levels of $E_{g1}{}^{1D}(k_x)$ estimated from a vacuum shot are included in Fig. 2m–p. The evaluated scaling for $E_{g1}{}^{1D}(k_x)$ in Fig. 2m is $k_x{}^{-3.0}$, close to the theoretical power law $k_\perp{}^{-10/3}$. The theoretical prediction $k_\perp{}^{-2}$ for the inertial range in the larger scale than the driving scale becomes dominant as $k_{\rm drive}\rho_{\rm thi}$ increases. The exponent evaluated for the measured $E_{g1}{}^{1D}(k_x)$ in Fig. 2p is $k_x{}^{-1.8}$. The observed behavior of these power laws in W_{g1} and E_g is consistent with the theory based on the hypothesis of dual self-similarity and the dual cascade of the entropy and field energy of the gyrokinetic system[20]. Our result strongly supports the validity of the dual-self similar hypothesis of gyrokinetic turbulence.

Note that the nonlinear decorrelation time[16,26] for these states is evaluated as $\tau_\rho \sim 10 \times 10^{-5}$ s; hence, the dimensionless parameter[16,26], which represents the scale separation analogous to Reynolds number, $D \sim 30$–40. Accordingly, the cutoff wavenumber, above which the collisional dissipation dominates the cascade, $k_{cut}\rho_{\rm thi} \sim 2D^{3/5} \sim 20$. This guarantees that the observed power-law spectral range corresponds to the inertial subrange.

In what follows, we discuss the applicability of the gyrokinetic theory and its impact on the interpretation of the experimental results. The theoretical aspects of the applicability of gyro kinetics to space and astrophysical plasmas are discussed in previous works[15,18,23]. In brief, strong magnetization, anisotropy, small amplitude, low fluctuation frequencies, equilibrium Maxwellian distribution, and nonrelativistic effects are assumed.

As described in Experimental setup, our experiment does not completely satisfy the strong magnetization condition $\omega \ll \Omega_{\rm ci}$ in consideration of the two adverse impacts of the strong field on our plasma states. One possible influence of this incomplete satisfaction of the gyrokinetic ordering is the possibility of stochastic ion heating[32,33]. According to ref. [34], the amplitude threshold for strong stochastic heating when $\beta < 1$ can be expressed in terms of the quantity $\varepsilon_{\rm i} \sim q_{\rm i}\delta\Phi_{\rm i}/mv^2$, where β, $q_{\rm i}$, and $\delta\Phi_{\rm i}$ are the thermal pressure normalized by the magnetic field pressure, electric charge of the ions, and root mean square amplitude of the electrostatic potential fluctuation at $k_\perp\rho_{\rm thi} \sim 1$, respectively. In our case, $\varepsilon_{\rm i} \sim 0.2$; therefore, the influence of stochastic ion heating is considered to be small. Ion cyclotron resonance heating is negligible because $\omega \not\gg \Omega_{\rm ci}$.

One of the weakest points of the gyrokinetic theory is the use of a Maxwellian as F_0[15]. Therefore, highly nonequilibrium turbulent states are not subjects of gyrokinetic theory. Nevertheless, the gyrokinetic theory is in effect in a wide range of space and turbulent astrophysical plasmas, as shown in numerous numerical simulations and theoretical considerations. Although our measurement has not had sufficient accuracy to be able to discuss a degree of deviation of F_0 from a Maxwellian distribution (Fig. 3d in "Methods" shows an example of the velocity distribution F_0), we believe that F_0 of our plasmas is not that different from a Maxwellian because of the following reasons: (i) no mechanisms that heat preferentially ions with specific velocity components exist; the collisional energy transfer caused by electron–ion collisions is the only possible heating source of ions; and (ii) ions are weak collisional, but not too weak. The mean-free path of ions for ion–ion collision is ~0.5 m < 1.6 m ~ L, which is the length of the plasma column. For the same reasons, pressure anisotropy is not considered.

The influence of the electron behavior on the entropy cascade in the ion phase space is considered negligible according to gyrokinetic numerical simulations[4,16,23]. The work done by Tatsuno et al. showed that no essential difference was observed between the cases of applying Boltzmann-response (3D) and no-response (2D) electrons in their simulations[4]. For more detailed electron energetics, please see, the work by Kawazura et al.[23], which studied the partition of irreversible heating between ions and electrons in terms of a compressive drive using hybrid gyrokinetic simulations.

Conclusions. In laboratory experiments, we present the measurement results of the Gibbs entropy distribution in the phase space of ions in electrostatic gyrokinetic turbulence. We confirm good agreement between the measurement and the theoretical prediction with a dual self-similar hypothesis in the scaling laws of the spectra of the entropy and the electric field energy. This result indicates an interplay between the position and velocity spaces of ions by perpendicular nonlinear phase mixing accompanied by a cascade of entropy in the phase space. Excitation of spectral components of the free energy W_{g1} with $k_\perp \sim p$ in the phase space gives evidence of nonlinear phase mixing at sub-Larmor scales. This observation corroborates the evidence of the existence of dual self-similarity and the dual-cascade of entropy and field energy.

An entropy cascade via nonlinear phase mixing is considered universal in magnetized plasma turbulence because it has been witnessed in various numerical simulations in different magnetized turbulence setups, including 2D[16] and 3D electrostatic[21], 3D electromagnetic turbulence, including the Alfvenic solar wind[4,22], and a simulation targeting an Alfvenic hot accretion disk[23]. The essential physical components in entropy cascades via nonlinear phase mixing include the gyro motion of the particles at the sub-Larmor scales and the interaction between the particles and the electrostatic fluctuations in addition to the strong anisotropy ($k_\perp \gg k_{||}$). Our experiment prepares turbulent states with these essential components in a simplified setup. Therefore, although our turbulence setup is in a narrow range (electrostatic turbulence in a drift-kinetic regime), our result is crucial for verifying universality. We believe that verifying the entropy cascades via nonlinear phase mixing contributes to understanding turbulent heating in the solar corona, solar wind, accretion disks, and magnetically confined fusion plasmas.

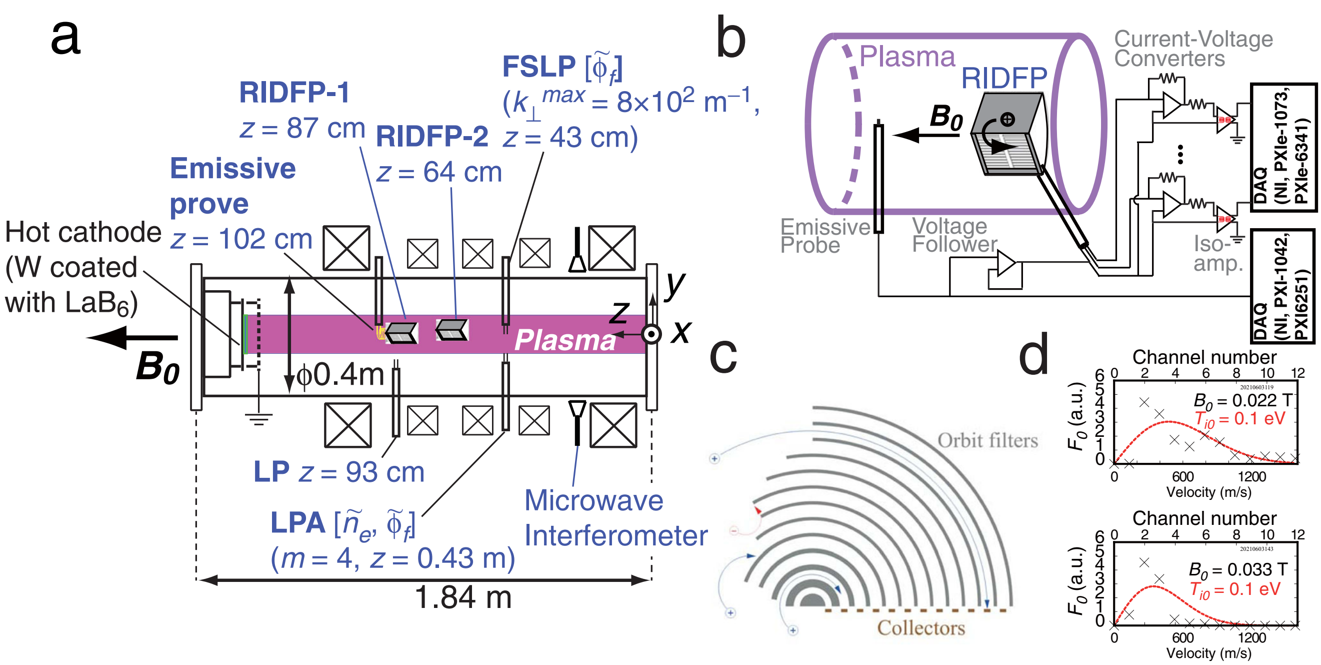

Fig. 3 Experimental setup. a Schematic diagram of the MPX plasma device including diagnostic systems. **b** System diagram of RIDFP (Ring-averaged ion velocity distribution function probe). **c** Schematic of the orbit filters and collector of the incoming gyrating ions. **d** Examples of equilibrium ring-averaged ion velocity distribution functions F_0 at a fixed guiding center position for the background magnetic field strength $B_0 = 0.022$ T and $B_0 = 0.033$ T, respectively. The red solid curves indicate Maxwellian having the temperature of 0.1 eV. Shrink of orbits of the ions (Larmor radii) for the B_0 change from 0.022 T to 0.033 T can be clearly observed, indicating validity of RIDFP measurement.

Methods

Magnetized plasma experiment (MPX) device: experimental device. The experiment was conducted in the MPX device[35] (Fig. 3a), which can prepare qualified plasma configurations for our purposes, namely, quasi-2D configurations with the magnetic field (the strength is denoted by B_0), the density, and temperatures within the target ranges. The hot cathode generated plasmas with the introduction of argon gas as the working gas. $g(\mathbf{R}, v_\perp)$ was measured by two RIDFPs separated by 3 mm and 230 mm in the x- and the z-directions, respectively (Fig. 3a), to obtain perpendicular wavenumbers $k_\perp$ of $g(\mathbf{R}, v_\perp)$ with the use of a two-point correlation technique[36]. RIDFPs were positioned at the center axis of the target plasmas to minimize the influence of steady $\mathbf{E} \times \mathbf{B}$ rotation of the plasmas. Figure 3 shows the equilibrium ring-averaged ion velocity distribution functions F_0 for $B_0 = 0.022$ T and $B_0 = 0.033$ T, respectively. The red solid curves indicate Maxwellian with a temperature of 0.1 eV. It can be observed that the orbits of the ions (Larmor radii) shrink as B_0 change from 0.022 T to 0.033 T, indicating the validity of the RIDFP measurement.

Ring-averaged ion velocity distribution function probes[28]. The RIDFP is a set of ion collectors that detect different velocity components and is immersed into magnetized plasmas. The RIDFP achieves momentum selection of incoming ions by selection of the ion Larmor radii by the orbit filter. To nullify the influence of the sheath potential surrounding the RIDFP on the incoming ions' orbits, the RIDFP body's electrostatic potential is automatically adjusted to coincide with the space potential of the target plasma with the use of an emissive probe and a voltage follower[28].

For precise measurement of the fluctuation $g(\mathbf{R}, v_\perp)$ in time, the ground potential of the current detection circuits is adjusted to that of the RIDFP body in order to eliminate capacitive coupling between the ion collectors and the RIDFP body. The length of RIDFP $L = 79$ mm satisfies the condition of $v_{||} {f_{ci}}^{-1} > L$, where $v_{||}$ is the parallel component of the thermal velocity of ions. This inequation imposes a condition for the plasma (ions) residing in the magnetic flux tube, in which an RIDFP is allocated, not to being severed by the RIDFP.

In the experiments, the resolution of the RIDFP measurement in the p-space $\Delta(pv_{thi})$ can be evaluated as follows: $\Delta pv_{upper\_bound} \sim \Delta p(2v_{thi}) = j_0 \fallingdotseq 2.4, \therefore \Delta p \fallingdotseq 1.2/v_{thi} \therefore \Delta(pv_{thi}) \sim 1.2$, where v_{upper_bound} and j_0 are the upper bounds of the measurable ion velocity by RIDFP and the first zero of the Bessel function of the first kind, respectively. The maximum (pv_{thi}) in the RIDFP measurement is obtained as: $(pv_{thi})_{max} \sim j_0 v_{thi}/\Delta v \sim 20$.

The other measurement tools and the plasma parameters. In addition to RIDFPs, we employed a few sets of Langmuir probes (LPs) for different purposes. An LP measured the plasma density in addition to a microwave interferometer[37]. The LP also measured the electron temperature and the space potential of the plasmas. A poloidal array of LPs named LPA diagnosed the macroscopic poloidal structures of fluctuations of ion saturation current and their floating potential. Another set of LPs named fine-scale LP (FSLP) was applied to measure the fluctuation of floating potential $\tilde{\phi}_f \approx \tilde{\phi}$ as functions of frequencies f and k_y (k_x), whose upper bound of measurable $k_\perp$ is ~$8 \times 10^2\,\mathrm{m}^{-1}$.

The hot cathode generated plasmas with the introduction of argon gas as the working gas. The typical plasma density and temperature are $n_e \sim 0.5\text{–}5 \times 10^{16}\,\mathrm{m}^{-3}$ and $T_e \sim 1\text{–}5$ eV, respectively, with a 15–20 cm diameter. Accordingly, the characteristic frequencies of the ion cyclotron f_{ci}, drift-wave f_{DW}, ion–ion Coulomb collisions f_{ii}, and ion-neutral collisions f_{in} have the following numbers:

$f_{ci} := \Omega_{ci}/2\pi \approx 8.4\,\mathrm{kHz} > f_{DW} \sim 1\text{–}4\,\mathrm{kHz} \sim f_{ii} \sim 1\text{–}5\,\mathrm{kHz} > f_{in} \sim 0.1\text{–}0.5\,\mathrm{kHz}$, where Ω_{ci} is the ion cyclotron angular frequency of singly ionized argon ion.

Evaluation of 1D spectrum of free energy $W_{g1}{}^{1D}(k_x, p)$ and relationship with $W_{g1}(k_\perp)$ and $W_{g1}(p)$. From the RIDFP measurement, 1D spectrum of free energy $W_{g1}{}^{1D}(k_x, p) \equiv \pi p \int_{-\infty}^{\infty} |g(\mathbf{k}_\perp, p)|^2 dk_y = \pi p \int_{-\infty}^{\infty} |g(k_x, k_y, p)|^2 dk_y$ is evaluated as follows, where: $g(\mathbf{k}_\perp, p) \equiv \frac{1}{2\pi} \int_{\mathbb{R}} d^2\mathbf{R} \int_0^{v_\perp^{upper}} v_\perp dv_\perp J_0(pv_\perp) e^{-i\mathbf{k}_\perp \cdot \mathbf{R}} g(\mathbf{R}, v_\perp)$

(1) Application of the Hankel transform concerning ion velocity $v_\perp$ to $g(\mathbf{R}_0, v_\perp, t)$ and $g(\mathbf{R}_0 + \Delta\mathbf{x}, v_\perp, t)$ measured by RIDFP-1 and RIDFP-2 gives $g(\mathbf{R}_0, p, t) \equiv \frac{1}{2\pi} \int_0^{v_\perp^{upper}} v_\perp dv_\perp J_0(pv_\perp) g(\mathbf{R}_0, v_\perp, t)$ and $g(\mathbf{R}_0 + \Delta\mathbf{x}, p, t)$, where $\mathbf{R}_0$ and $\mathbf{R}_0 + \Delta\mathbf{x}$ are the positions of the guiding center of RIDFP1 and RIDFP2, respectively.

(2) Fourier transforms of $g(\mathbf{R}_0, p, t)$ and $g(\mathbf{R}_0 + \Delta\mathbf{x}, p, t)$ about time t are applied to obtain $g(\mathbf{R}_0, p, f, \theta)$ and $g(\mathbf{R}_0 + \Delta\mathbf{x}, p, f, \theta)$, where θ represents the phase of the component of the frequency f.

(3) Wavenumbers k_x for all p-components are calculated by applying the two-point correlation technique to $g(\mathbf{R}_0, p, f, \theta)$ and $g(\mathbf{R}_0 + \Delta\mathbf{x}, p, f, \theta)$. Integration of those about f gives $\int_{-\infty}^{\infty} |g(k_x, k_y, p)|^2 dk_y = W_{g1}{}^{1D}(k_x, p)/(\pi p)$.

If turbulence is isotropic, $W_{g1}{}^{1D}(k_x, p) = \pi p \int_{-\infty}^{\infty} |g(\sqrt{k_x^2 + k_y^2}, p)|^2 dk_y$. Applying a variable change $\tan\theta = \frac{k_y}{k_x}$ and a cutoff θ_{cut} for the upper bound of the integration, one can obtain

$$\boldsymbol{W_{g1}{}^{1D}(k_x, p) = 2p \int_0^{\theta_{cut}} \left| g\left(k_x\sqrt{1 + \tan\theta}, p\right)\right|^2 \frac{d\theta}{\cos^2\theta}} \tag{1}$$

When $W_{g1}(k_\perp) = \int k_\perp |g(k_\perp, p)|^2 dp \propto k_\perp{}^{-\alpha}$, $W_{g1}{}^{1D}(k_x) = \int W_{g1}{}^{1D}(k_x, p) dp \propto k_x{}^{-\alpha}$.

$$\boldsymbol{W_{g1}(k_\perp, p) \equiv p \sum_{|\mathbf{k}_\perp| = k_\perp} |g(\mathbf{k}_\perp, p)|^2 = \pi k_\perp p |g(k_\perp, p)|^2}. \tag{2}$$

Then,

$$\begin{aligned}W_{g1}(p) \equiv \pi p\int_0^{\infty}\sum_{|\mathbf{k}_\perp|=k_\perp}|g(\mathbf{k}_\perp,p)|^2dk_\perp = \pi p\iint_{-\infty}^{\infty}|g(k_x,k_y,p)|^2dk_ydk_x \\ = \int_{-\infty}^{\infty}W_{g1}{}^{1D}(k_x,p)dk_x\end{aligned} \tag{3}$$

Evaluation of the 1D spectrum of the electrostatic field energy $E_g{}^{1D}(k_y)$ and its relationship with $E_g(k_\perp)$. From the FSLP measurement, the 1D spectrum of the electrostatic field energy $E_g{}^{1D}(k_y) \equiv \int_{-\infty}^{\infty}|\tilde{\phi}(\mathbf{k}_\perp)|^2dk_x$ is evaluated as follows:

If turbulence is isotropic, $E_g{}^{1D}(k_y) = \int_{-\infty}^{\infty}|\tilde{\phi}(\sqrt{k_x^2+k_y^2})|^2dk_x$. Applying a variable change $\tan\theta = \frac{k_y}{k_x}$ and a cutoff θ_{cut} for the upper bound of the integration, one can obtain

$$E_g{}^{1D}(k_y) = 2\int_0^{\theta_{cut}}\left|\tilde{\phi}\left(k_x\sqrt{1+\tan\theta}\right)\right|^2\frac{d\theta}{\cos^2\theta}. \tag{4}$$

When $E_g(k_\perp) \propto k_\perp{}^{-\alpha}$, $E_g{}^{1D}(k_y) = \int E_g(k_\perp)dk_x \propto k_y{}^{-\alpha}$.

Data availability

The data supporting this study's findings are available from the corresponding author upon reasonable request.

Received: 16 April 2022; Accepted: 9 December 2022;
Published online: 27 December 2022

References

1. Kolmogorov, A. N. The local structure of turbulence in incompressible viscous fluid for very large Reynolds' numbers. *Dokl. Akad. Nauk SSSR* **30**, 301–305 (1941).
2. Kraichnan, R. H. Inertial ranges in two-dimensional turbulence. *Phys. Fluids* **10**, 1417 (1967).
3. Champagne, F. H. The fine-scale structure of the turbulent velocity field. *J. Fluid Mech.* **86**, 67–108 (1978).
4. Howes, G. G. et al. Gyrokinetic simulations of solar wind turbulence from ion to electron scales. *Phys. Rev. Lett.* **107**, 035004 (2011).
5. Chen, C. H. K. et al. The evolution and role of solar wind turbulence in the inner heliosphere. *ApJS* **246**, 53 (2020).
6. McComas, D. J. et al. Understanding coronal heating and solar wind acceleration: case for in situ near-Sun measurements. *Rev. Geophysics* **45**, RG1004 (2007).
7. Cranmer, Steven, R. et al. The role of turbulence in coronal heating and solar wind expansion. *Philos. Trans. R. Soc. A* **373**, 20140148 (2015).
8. Chandran, B., Foucart, F. & Tchekhovskoy, A. Heating of accretion-disk coronae and jets by general relativistic magnetohydrodynamic turbulence. *J. Plasma Phys.* **84**, 905840310 (2018).
9. Sharma, P., Quataert, E., Hammett, G. W. & Stone, J. M. Electron heating in hot accretion flows. *Astrophys. J.* **667**, 714–723 (2007).
10. Rossi, E. M., Armitage, P. J. & Menou, K. Microphysical dissipation, turbulence and magnetic fields in hyper-accreting discs. *Monthly Not. R. Astronomical Soc.* **391**, 922–934 (2008).
11. Krommes, J. A. & Hu, G. The role of dissipation in the theory and simulations of homogeneous plasma turbulence, and resolution of the entropy paradox. *Phys. Plasmas* **1**, 3211 (1994).
12. Watanabe, T.-H. & Sugama, H. Kinetic simulation of steady states of ion temperature gradient driven turbulence with weak collisionality. *Phys. Plasmas* **11**, 1476 (2004).
13. Howard, N. T. et al. The role of ion and electron-scale turbulence in setting heat and particle transport in the DIII-D ITER baseline scenario. *Nucl. Fusion* **61**, 106002 (2021).
14. Schekochihin, A. A. et al. Gyrokinetic turbulence: a nonlinear route to dissipation through phase space. *Plasma Phys. Control. Fusion* **50**, 124024 (2008).
15. Schekochihin, A. A. et al. Astrophysical gyrokinetics: kinetic and fluid turbulent cascades in magnetized weakly collisional plasmas. *ApJS* **182**, 310 (2009).
16. Tatsuno, T. et al. Nonlinear phase mixing and phase-space cascade of entropy in gyrokinetic plasma turbulence. *Phys. Rev. Lett.* **103**, 015003 (2009).
17. Frieman, E. A. & Chen, L. Nonlinear gyrokinetic equations for low-frequency electromagnetic waves in general plasma equilibria. *Phys. Fluids* **25**, 502 (1982).
18. Howes, G. G. et al. Astrophysical gyrokinetics: basic equations and linear theory. *ApJ* **651**, 590–614 (2006).
19. Dorland, W. & Hammett, G. W. Gyrofluid turbulence models with kinetic effects. *Phys. Fluids B* **5**, 812–835 (1993).
20. Plunk, G., Cowley, S., Schekochihin, A. & Tatsuno, T. Two-dimensional gyrokinetic turbulence. *J. Fluid Mech.* **664**, 407–435 (2010).
21. Navarro, A. B. et al. Free energy cascade in gyrokinetic turbulence. *Phys. Rev. Lett.* **106**, 055001 (2011).
22. Navarro, A. B. et al. Structure of plasma heating in gyrokinetic Alfvénic turbulence. *Phys. Rev. Lett.* **117**, 245101 (2016).
23. Kawazura, Y. et al. Ion versus electron heating in compressively driven astrophysical gyrokinetic turbulence. *Phys. Rev. X* **10**, 041050 (2020).
24. Servidio, S. et al. Magnetospheric multiscale observation of plasma velocity-space cascade: hermite representation and theory. *Phys. Rev. Lett.* **119**, 205101 (2017).
25. Plunk, G. & Tatsuno, T. Energy transfer and dual cascade in kinetic magnetized plasma turbulence. *Phys. Rev. Lett.* **106**, 165003 (2011).
26. Tatsuno, T. et al. Gyrokinetic simulation of entropy cascade in two-dimensional electrostatic turbulence. *J. Plasma Fusion Res. Ser.* **9**, 509 (2010).
27. Kolmogorov, A. N. Dissipation of energy in the locally isotropic turbulence. *Dokl. Akad. Nauk SSSR* **32**, 16–18 (1941).
28. Kawamori, E., Chen, J., Lin, C. & Lee, Z. Ring-averaged ion velocity distribution function probe for laboratory magnetized plasma experiment. *Rev. Sci. Instrum.* **88**, 103507 (2017).
29. Kawamori, E. Experimental verification of entropy cascade in two-dimensional electrostatic turbulence in magnetized plasma. *Phys. Rev. Lett.* **110**, 095001 (2013).
30. Sasaki, M., Kasuya, N., Itoh, K., Yagi, M. & Itoh, S.-I. Nonlinear competition of turbulent structures and improved confinement in magnetized cylindrical plasmas. *Nucl. Fusion* **54**, 114009 (2014).
31. Chang, F.-J. & Kawamori, E. Control of solitary-drift-wave formation by radial density gradient in laboratory magnetized cylindrical plasma. *Phys. Plasmas* **26**, 072304 (2019).
32. Chandran, B. D. G. Alfvén-wave turbulence and perpendicular ion temperatures in coronal holes. *ApJ* **720**, 548 (2010).
33. Cerri, S. S., Arzamasskiy, L. & Kunz, M. W. On stochastic heating and its phase-space signatures in low-beta kinetic turbulence. *Astrophysical J.* **916**, 120 (2021).
34. Chandran, B. D. G. et al. Perpendicular ion heating by low-frequency Alfvén-wave turbulence in the solar wind. *ApJ* **720**, 503 (2010).
35. Kawamori, E. et al. Lithium plasma emitter for collisionless magnetized plasma experiment. *Rev. Sci. Instrum.* **82**, 093502 (2011).
36. Beall, J. M., Kim, Y. C. & Powers, E. J. Estimation of wavenumber and frequency spectra using fixed probe pairs. *J. Appl. Phys.* **53**, 3933 (1982).
37. Kawamori, E., Lin, Y., Mase, A., Nishida, Y. & Cheng, C. Z. Multichannel microwave interferometer with an antenna switching system for electron density measurement in a laboratory plasma experiment. *Rev. Sci. Instrum.* **85**, 023507 (2014).

Acknowledgements

This work was supported by Grants-in-Aid MOST 111-2112-M-006-025 from the Ministry of Science and Technology, Taiwan.

Author contributions

E.K. designed the study and approaches. Y.L. designed the upgraded version of RIDFPs. Y.L. and E.K. performed the optimization experiments of the RIDFPs. E.K. and Y.L. developed the diagnostic tools. E.K. performed the experiments, measurements and analysis. E.K. and Y.L. wrote the paper. E.K. supervised the study.

Competing interests

The authors declare no competing interests.

Additional information

Correspondence and requests for materials should be addressed to Eiichirou Kawamori.

Peer review information *Communications Physics* thanks the anonymous reviewers for their contribution to the peer review of this work.

Reprints and permission information is available at http://www.nature.com/reprints

Publisher's note Springer Nature remains neutral with regard to jurisdictional claims in published maps and institutional affiliations.

Open Access This article is licensed under a Creative Commons Attribution 4.0 International License, which permits use, sharing, adaptation, distribution and reproduction in any medium or format, as long as you give appropriate credit to the original author(s) and the source, provide a link to the Creative Commons license, and indicate if changes were made. The images or other third party material in this article are included in the article's Creative Commons license, unless indicated otherwise in a credit line to the material. If material is not included in the article's Creative Commons license and your intended use is not permitted by statutory regulation or exceeds the permitted use, you will need to obtain permission directly from the copyright holder. To view a copy of this license, visit http://creativecommons.org/licenses/by/4.0/.

© The Author(s) 2022